Orientation and morphology of Pt nanoparticles in γ-alumina processed *via* ion implantation and thermal annealing

Arielle L. Clauser[a], Raquel Giulian[b], Zachary D. McClure[c,e], Kofi Oware Sarfo[c], Colin Ophus[d], Jim Ciston[d], Líney Árnadóttir[c], Melissa K. Santala[a,*]

[a] School of Mechanical, Industrial, and Manufacturing Engineering, Oregon State University, 204 Rogers Hall, Corvallis, OR 97331-6001, United States
[b] Institute of Physics, Federal University of Rio Grande do Sul, Porto Alegre, Brasil
[c] School of Chemical, Biological, and Environmental Engineering, Oregon State University, Corvallis, OR, United States
[d] National Center for Electron Microscopy, Molecular Foundry, Lawrence Berkeley National Laboratory, Berkeley, CA, United States
[e] School of Materials Engineering & Birck Nanotechnology Center, Purdue University, West Lafayette, IN, United States

ARTICLE INFO

ABSTRACT

Structure and chemistry of metal/metal-oxide interfaces are critical for many catalytic processes and sensing. Pristine interfaces of Pt and γ-Al_2O_3 were fabricated using high-energy ion implantation and thermal processing. Amorphous regions of alumina develop in single crystal α-alumina during Pt^+ implantation and an 800 °C thermal treatment crystalizes amorphized alumina to γ-Al_2O_3 and allows Pt ions to precipitate within the developing γ-alumina, yielding Pt nanoparticle tetrahedra terminated by {111} surfaces. The phase of alumina that developed and the distribution, morphology, and orientation of Pt nanoparticles was determined using x-ray diffraction, Rutherford backscattering spectrometry, transmission electron microscopy and scanning transmission electron microscopy.

© 2020 Acta Materialia Inc. Published by Elsevier Ltd. All rights reserved.

The formation of nanoprecipitates by high-dose ion implantation followed by thermal annealing is a means to alter the near-surface optical, electrical, and magnetic properties of oxides and other insulators and has potential technological applications [1,2]. The size and spatial distribution of the nanoprecipitates can be controlled by the implantation dose, energy, and annealing temperature and environment. These parameters also impact the level of damage to the matrix and the path of recovery during thermal annealing which in turn can alter the orientation relationships of the precipitates [3]. This provides an opportunity to tune properties [4] and also a platform for studying of metal/oxide interfaces with a variety of interfacial relationships [5]. In this work, high-energy ion implantation of platinum into sapphire (α-Al_2O_3) wafers followed by thermal annealing was used to create a simple, model system of dense γ-alumina with Pt nanoparticles for detailed characterization of orientation relationships, interfacial relationships, and nanoparticle morphology. Platinum dispersed on γ-alumina is an important heterogeneous catalyst system [6,7]. The orientation, size, and morphology of metal nanoparticles on oxide supports impact the activity of heterogeneous catalyst systems [8,9], but characterization of Pt nanoparticles on γ-alumina is chal-lenging due to the complexity of γ-alumina and the added degrees of freedom introduced by the nanoparticles. This model system differs substantially from those used for heterocatalysis because the nanoparticles are embedded in the oxide, however its simplicity offers a path to study the atomic-level structure of Pt/γ-alumina interfaces. The identification of faceted interfaces with an interfacial relationship common to those observed in supported nanoparticles gives direction for studies on the atomic-level characterization of the interfaces.

The γ-alumina phase is a transition alumina that may be produced by different processing paths, including the topotactic transformation of boehmite [10] or crystallization of amorphous Al_2O_3 [11]. The structure of γ-alumina has been the subject of experimental investigations [10-14] and computational simulations [15-19] and yet is still debated. X-ray diffraction (XRD) [10,11] and other characterization experiments may be inconclusive because of the structural similarities between γ-alumina and other transition aluminas and the frequent co-existence of different alumina phases. Numerous models for γ-alumina have been proposed, including Zhou and Snyder's defect spinel Fd$\bar{3}$m model derived from XRD and Rietveld refinement of neutron diffraction data [12], a proposed refinement of that model with a tetragonal I41/*amd* structure [17,19], and a model with modifications to capture the properties of γ-alumina surfaces [18]. Transmission electron mi-

* Corresponding author.
E-mail address: melissa.santala@oregonstate.edu (M.K. Santala).

croscopy (TEM) diffraction and high-resolution (HR) imaging have been used to study the structure of γ-alumina and distinguish it from the similar δ- and θ-alumina forms [11,20-24].

Ion implantation of Pt into sapphire followed by thermal annealing has been used to produce Pt nanoparticles in γ-alumina [3], θ-alumina [25,26], and α-alumina [3,5,25-27]. Accumulation of damage during ion implantation can result in near-surface amorphization of the sapphire matrix. Annealing induces re-crystallization of the amorphized alumina and precipitation of the implanted Pt. The form of alumina after re-crystallization is determined by the annealing conditions. Upon heating, the expected transitions of amorphous alumina are $\gamma \rightarrow \delta \rightarrow \theta \rightarrow \alpha$ [11]. These transitions are not reversible upon cooling. While the thermodynamic and kinetic factors influencing the orientation and morphology of Pt with γ-alumina differ between embedded and supported nanoparticles, the study of interfaces in a model system using embedded nanoparticles produced by this processing method provides certain advantages. Topotaxial re-growth of alumina has been reported for γ/α [3,28,29] and θ/α-alumina [25] interfaces formed during re-crystallization of partially amorphized α-alumina. The resulting interfacial relationships have the parallel closed-packed planes of oxygen and parallel alignment of the close-packed oxygen directions. The well-defined orientation relationship of the re-crystallized alumina with the undamaged sapphire matrix greatly simplifies the systematic study of the structure of many nanoparticles through atomic-resolution zone axis imaging.

Introducing Pt sub-surface *via* ion implantation offers great control over the system purity and distribution of the metal. The accumulated damage in the alumina is controlled through the implantation energy, fluence, and substrate temperature. The specimen purity is limited only by the base impurities of the γ-alumina "precursor", sapphire, which is commercially available with impurity levels under 100 parts per million. The formation of nanoparticles within the alumina, without a pre-existing alumina interface also allows, by comparison, an evaluation of the role of surface orientation on the orientation relationships and interfacial relationships observed in supported particles.

When Pt implanted into alumina precipitates, the orientation relationships that develop depend on the phase of alumina [5,25-27,30,31]. Precipitation into α-alumina results in multiple orientations of Pt nanoparticles, whereas precipitation of Pt into a θ-alumina at 1000 °C leads to a single predominant orientation relationship, $(111)_{Pt}||(\bar{2}01)_{\theta\alpha}$;$[1\bar{1}0]_{Pt}||[132]_{\theta}$, [25,26] in which the close-packed $\{111\}_{Pt}$ planes are parallel with close-packed planes of the oxygen sub-lattice. These Pt nanoparticles in θ-alumina are bound by $\{111\}_{Pt}$ facets [26]. The structure of θ-alumina is related to γ-alumina in its near face-center-cubic packing of the oxygen sublattice, but has a monoclinic, rather than cubic crystal structure. This orientation and morphology results in multiple close-packed directions to be in parallel alignment at the interfaces.

Pt nanoparticles embedded in alumina were produced via ion implantation and thermal annealing of 99.99% pure optical grade sapphire wafers with [0001] direction normal to the wafer face. The alumina was partially amorphized by implantation of 600 keV Pt$^+$ ions at 7° to the normal of the sapphire wafer at room temperature. Two wafers were implanted in a 300 kV Tandetron at the Ion Implantation Laboratory at UFRGS with target fluences of 5×10^{16} Pt$^+$ions/cm^2 and 1×10^{17} Pt$^+$ions/cm^2. Both fluences are high enough to amorphize the near-surface region of the implanted sapphire. Higher fluences at the same implantation energy increases the local sub-surface density of the implanted species and decreases the diffusion distances required for the formation of nanoparticles and was expected to result in a higher density of nanoparticles. The implantation energy was expected to result in a peak density of Pt at 94.1 nm below the Al$_2$O$_3$ surface, based on calculations performed with the Stopping and Range of Ions in
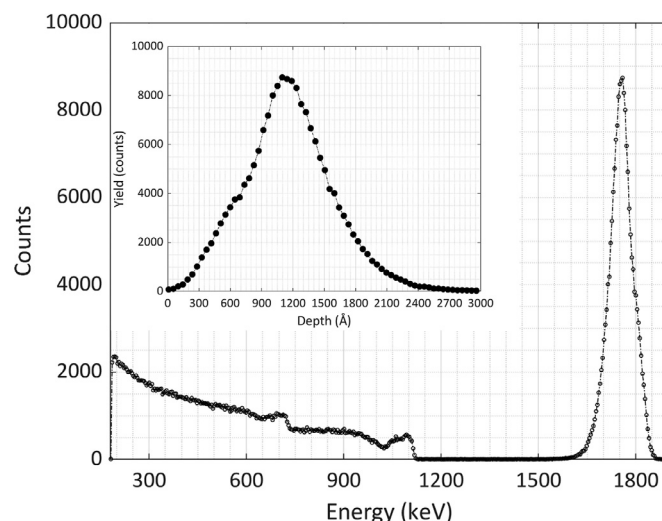

Fig. 1. RBS spectrum used to determine the depth and Pt fluence in the sapphire wafer with a target fluence of 1×10^{17} Pt/cm^2 before thermal treatment. The peak concentration of Pt occurred at a depth of 110 nm and fluence was found to vary over the wafer, ranging between 0.8 and 2×10^{17} Pt$^+$/cm^2.

Matter software (SRIM) [32]. Rutherford backscattering spectrometry (RBS) was used to characterize the depth of the implanted Pt and to verify the implantation fluences in the two as-implanted wafers. RBS measurements were performed at the Ion Implantation Laboratory at UFRGS using 1 MeV He$^+$ ions and the backscattered ions were detected by a surface barrier detector. RUMP software (version 2.0) [33,34] was used to analyze the RBS data and calculate the depth distribution of Pt atoms and implantation fluence. A piece of each of the implanted wafers was annealed at 800 °C for 500 h in air with the goal of forming γ-alumina with well-defined Pt nano-precipitates. An annealing temperature of 800 °C was chosen as the highest temperature expected to induce crystallization to γ-alumina without transition to δ-alumina [10,13]. XRD was used to characterize changes in near-surface crystal structure caused by implantation and subsequent thermal annealing. A Bruker AXS-D8 Discover diffractometer using Cu Kα radiation (wavelength 0.15406 nm) was used for $\theta-2\theta$ scans from 10 to 100° (2θ) at a scanning rate of 5°/min. After XRD, specimens were prepared for TEM by mechanically thinning of glued cross sections to ~100 μm, polishing one side to 0.25 μm grit, then dimpling and polishing the other side to a 0.25 μm grit finish, followed by Ar$^+$ milling to perforation. An FEI Titan TEM, operated at 200 keV, was used to collect bright-field (BF) and dark-field (DF) images and selected area electron diffraction (SAED) patterns. An image-corrected FEI Titan, operated at 300 keV, was used for high-resolution TEM (HRTEM) imaging. The TEAM I at the National Center for Electron Microscopy Facility of the Molecular Foundry at Lawrence Berkeley National Lab was operated at 300 keV to collect probe-corrected high-angle annular dark field (HAADF) scanning TEM (STEM) data.

RBS was performed at five points across the wafer that had a nominal target fluence of 1×10^{17} Pt/cm^2. The measured Pt fluence varied from a peak of 2×10^{17} Pt/cm^2 at the center of the wafer to 0.8×10^{17} Pt/cm^2, 10 mm away, near the edge of the wafer. The concentration profile of Pt as a function of depth was determined with RBS on the as-implanted wafer with a target fluence of 1×10^{17} Pt/cm^2. The RBS spectrum is shown in Fig. 1 and the inset shows the peak concentration was 110 nm below the wafer surface. XRD of the as-implanted specimen with nominally 1×10^{17} Pt/cm^2 (Fig. 2a) shows prominent peaks at $2\theta=41.8°$ and 90.8°, consistent with $(0006)_\alpha$ and $(000.12)_\alpha$ of α-alumina ex-
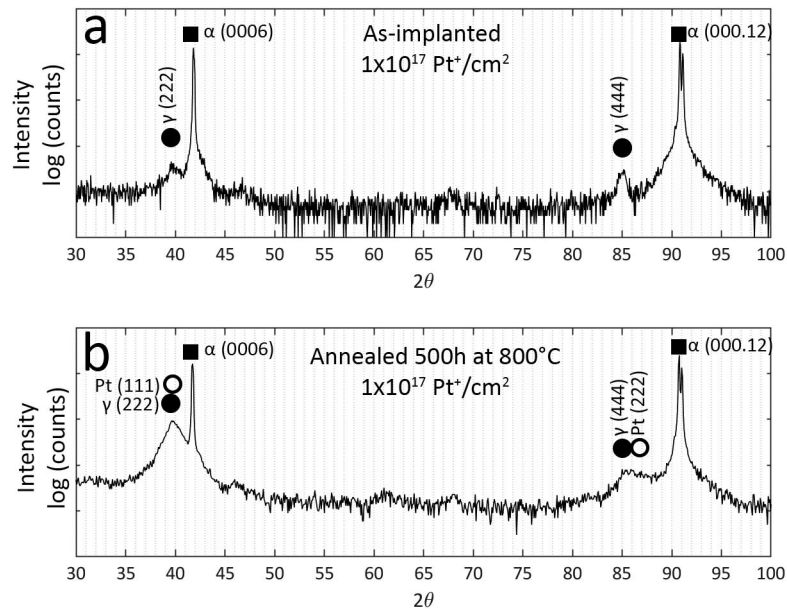
Fig. 2. XRD of sapphire wafers after implantation but before annealing (a) showing intense α-Al$_2$O$_3$ peaks and broad, weak peaks likely due to a transition alumina formed by implantation damage to the matrix. After 500 h at 800C (b), peaks consistent with Pt and a transition alumina are visible. The lack of other peaks is evidence of highly oriented growth of transition alumina and the consistent orientation of the Pt nanoparticles within the alumina. Identification of Pt and γ-alumina peaks is based on additional information from TEM imaging and diffraction.

pected from the bulk of the sapphire wafer. There are small peaks at 39.6° and 85.2° in the as-implanted specimen, which show a large increase in relative intensity with respect to the α-alumina peaks after 500 h at 800 °C along with broadening of the peak at $2\theta=85°$ (Fig. 2b). The observed peaks (and notable absence of others) are consistent with the development of γ-alumina and the precipitation of Pt with a well-defined in-plane orientation relative to the sapphire matrix. The $(222)_\gamma$ and $(111)_{Pt}$ peaks are expected at $2\theta =39.4°$ and 39.8°, respectively, and the $(444)_\gamma$ and $(222)_{Pt}$ peaks are expected at 85.0° and 85.7°, respectively. These peaks indicate $\{111\}_{Pt}$ and $\{222\}_\gamma$ planes are parallel to $(0006)_\alpha$ planes of the sapphire, but does not exclude other orientations that may not be detected in XRD if they present only at a very small phase fraction. Because of the similarity between transition phases of alumina, the presence of other forms cannot be excluded based on these XRD data. The assignment of the γ-alumina and Pt peaks in Fig. 2 was made using additional information derived from the TEM experiments described below.

TEM was used to characterize changes in the microstructure and the crystal structure with processing and to characterize the Pt-alumina orientation relationships and Pt nanoparticle morphology. Fig. 3a shows a cross section of a sapphire wafer as-implanted with 5×10^{16} Pt/cm^2. A nearly featureless, 133 ± 8 nm thick amorphous layer lies beneath an 86 ± 3 nm thick damaged α-alumina with the highest density of Pt at ~110 nm beneath the surface, in agreement with RBS data, and located within the amorphized layer of alumina. SRIM calculations, predict a peak concentration at a depth of only 94 nm, but this small discrepancy is not unexpected as the accuracy for predicting the stopping power of compound materials, such as aluminum oxide, are limited, as SRIM does not capture the change in the strength of interactions in the compound [32].

A BF zone-axis image (Fig. 3b) after 500 h at 800 °C shows dark Pt nanoparticles that have developed within the re-crystallized alumina in the implanted region. Most Pt nanoparticles are within the γ-alumina, because the peak Pt density from implantation was within the amorphous region. However, annealing also caused growth α-Al$_2$O$_3$ into the γ-alumina. The α-Al$_2$O$_3$ grows past some

Pt particles, which appear to have been dragged with the boundary. This process leaves some nanoparticles within the α-Al$_2$O$_3$ and some decorating the α/γ-alumina boundary, similar to the microstructural development of Pt-implanted α-Al$_2$O$_3$ annealed at 1000 °C, except in that case the transition form of the oxide is θ-alumina [25-27].

SAED was used to confirm the identity of transition alumina and to determine the prevalent orientation relationships between the phases. A two-beam DF image (Fig. 3c) was taken of the region using the overlapping 111_{Pt} and 222_γ diffracted beams and shows that nearly all Pt particles in the γ-alumina matrix are oriented with $(111)_{Pt}\|(222)_\gamma$, confirming that the in-plane orientation determined by XRD is prevalent. Fig. 3d shows a typical SAED from the implanted region of a specimen after annealing at 800 °C for 500 h. A simulated SAED [211] zone axis pattern for both Pt and the Zhou and Snyder γ-alumina model is shown in Fig. 3e and is an excellent match to the experimental pattern. This may reflect the fact that the diffraction information is derived from many cubic nanometers of the γ-alumina – higher resolution structural characterization may be required to reveal the tetragonal symmetry that is predicted by the work of Paglia and coworkers [17,19]. Based on reports on the alumina transition series [10,11], the processing path used here could plausibly result in δ-alumina, however TEM imaging and diffraction observations of these specimens differ substantially from other TEM characterization of δ-alumina [11,21,22]. As an example, a simulated pattern of δ-alumina, based on a structure from reference [22], shown down an equivalent zone axis to $[211]_\gamma$ in Fig. 3f shows expected diffraction intensity absent in Fig. 3d. This and other observations exclude δ-alumina as the transition phase in our specimens. Fig. 3d allows the prevalent orientation relationship between the Pt particles and γ-alumina to be fully determined as $(111)_{Pt}\|(111)_\gamma;[1\bar{1}0]_\gamma\|[1\bar{1}0]_{Pt}$, a "cube-on-cube" orientation.

Phase-contrast HRTEM was used to characterize the morphology and the faceted interfaces of the Pt nanoparticles in a specimen from the wafer with the higher density of nanoparticles (1×10^{17} Pt/cm^2, annealed 500 h at 800 °C). Fig. 4a shows an atomic resolution micrograph of Pt nanoparticles in a γ-alumina
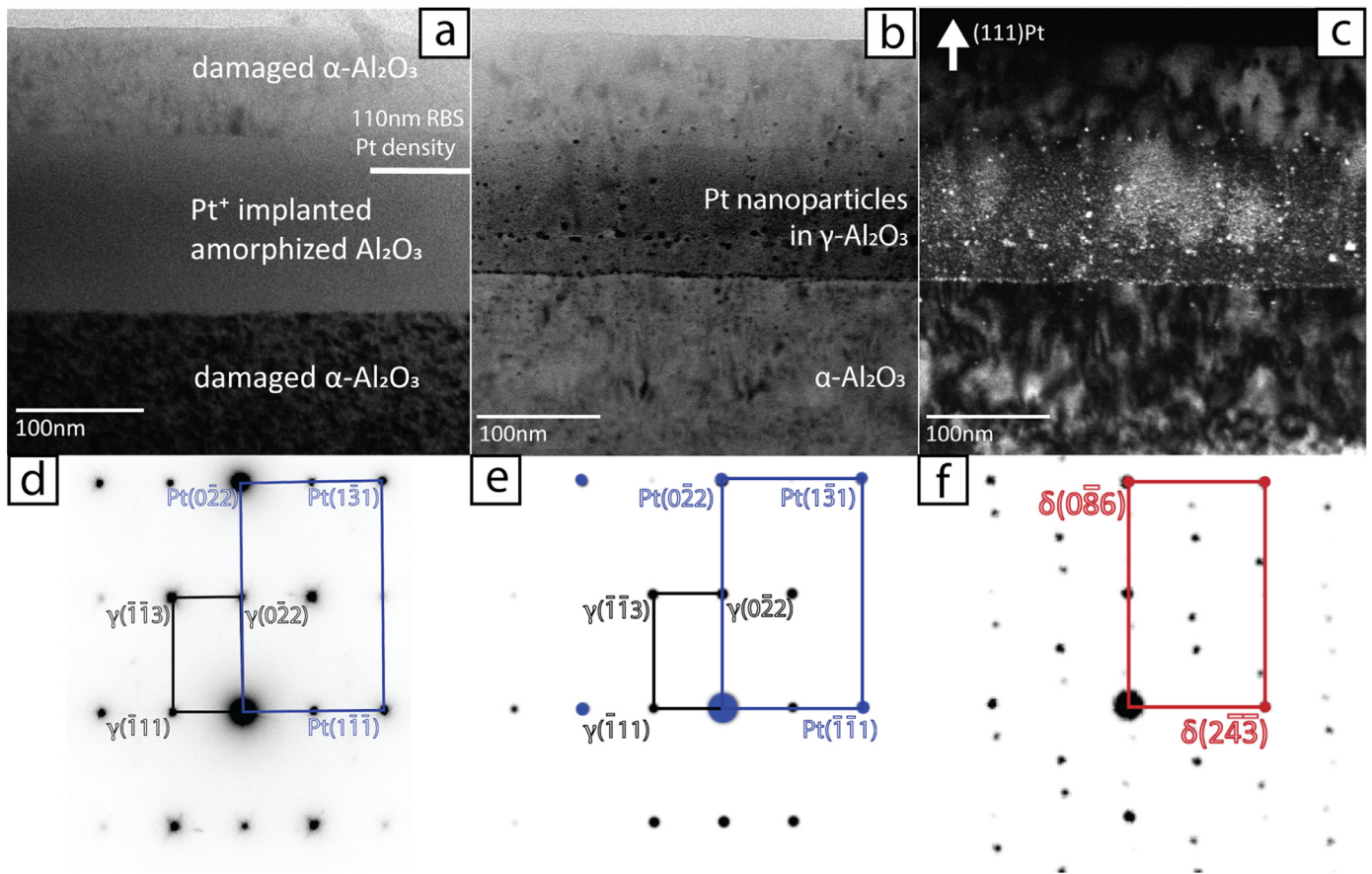
Fig. 3. BF TEM images of a cross section of (a) the as-implanted 5×10^{16} Pt/cm^2 wafer and (b) after 500 h at 800 °C. The sapphire is amorphized where the peak density of implanted Pt occurs. After 500 h at 800 °C (b), the amorphous alumina has recrystallized as γ-alumina and the α-alumina has grown into the region that had been amorphized. Most of the precipitates are near the peak of the implanted Pt density, but they also decorate the γ/α-alumina boundary. (c) DF image of the region in (b) taken in a two-beam condition from $(111)_{Pt}$ and $(222)_{\gamma}$; the smallest objective aperture could not exclude the $(0006)_{\alpha}$ diffracted beam. The DF image highlights the high degree of alignment of the Pt within the γ-alumina and of γ-alumina with the α phase. Experimental SAED pattern (d) of the implanted region after annealing at 800 °C for 500 h; the adjacent sapphire was excluded with the selected area aperture. The intensities were inverted for clarity. Simulated SAED patterns of (e) Pt and γ-alumina along the [211] zone axes, using the Zhou and Snyder model [12] and (f) of δ-alumina using a structure reported by Kovarik et al. [17] along the $[35.9.12]_{\delta}$ zone axis where $(\bar{2}43)_{\delta}$ is equivalent to $(\bar{1}11)_{\gamma}$ (parallel to close-packed planes of the oxygen sub-lattice) and $(0\bar{4}3)_{\delta}$ is to $(0\bar{2}2)_{\gamma}$.

matrix with the underlying α-alumina. Insets in Fig. 4a show fast Fourier transforms (FFTs) of image regions with Pt nanoparticles in γ-alumina (region 1) and the α-alumina (region 2) revealing the orientation relationships of the phases. The γ-alumina forms with the orientation $(0006)_{\alpha}||(111)_{\gamma}$; $[10\bar{1}0]_{\alpha}||[110]_{\gamma}$, which results in parallel alignment of close-packed planes of the oxygen sub-lattice in each of the phases as well as alignment of the close-packed oxygen directions within those planes at the interfaces. Epitaxial growth of γ-alumina on α-alumina has been documented after thermal annealing of α-alumina that had been partially amorphized by high-energy ion bombardment of various species [3,28]. The Pt particles have the orientation $(111)_{Pt}||(111)_{\gamma}$; $[1\bar{1}0]_{\gamma}||[1\bar{1}0]_{Pt}$ (as in the specimen with lower fluence) and many appear to be in the form of tetrahedra or truncated tetrahedra bound by {111} facets. The morphology of the nanoparticles was surveyed in HRTEM images of more than 30 particles. All the Pt nanoparticles showed prominent {111} facets, although some also presented small {002} facets.

The three-dimensional (3D) morphology of Pt nanoparticles may be more easily inferred from HAADF STEM image because image intensity is more directly related to scattering potential and the intensity of the Pt positions is roughly proportional to the number of Pt in the columns. The near tetrahedral form of small Pt nanoparticles can be inferred in atomic resolution HAADF STEM images (Fig. 4b). A schematic of the morphology of a perfect tetra-

hedral nanoparticle is shown in the inset of Fig. 4b. The smallest particles (one's containing ~100 Pt atoms) tend toward a defective tetrahedral shape rather than a cubo-octahedral, with symmetric {111} facets and {200} facets. The larger particles, which have not converged onto a single shape, are more likely to be cubo-octahedral in shape, as shown in the HRTEM image in Fig. 4c. The equilibrium shape is expected to be independent of size for large particles, but for small particles (<20 nm), the edge energies can be a significant contribution to the total interfacial energy, resulting in changes in the equilibrium shape as a function of size [35,36]. Additionally, strain energy may impact the morphology of precipitates as a function of size [37,38]. At this point, it is unclear if the difference in morphology of large and small nanoparticles is simply due to a lack of convergence of the larger particles onto a tetrahedral form, or if it is due to different relative contributions of strain, interfacial, and edge energies related to the nanoparticle size.

Orientation and interfacial relationships that develop during precipitation into a solid matrix and onto surfaces can differ because the strain and interfacial energetic contributions on embedded particles with 3D constraints differ from supported particles with two-dimensional constraints [39]. However, common interfacial orientation may still develop, which is the case for Pt and γ-alumina. Zhang et al. [40] reported that Pt nanoparticles supported on (111) γ-alumina surfaces, formed by oxidation of (110) NiAl
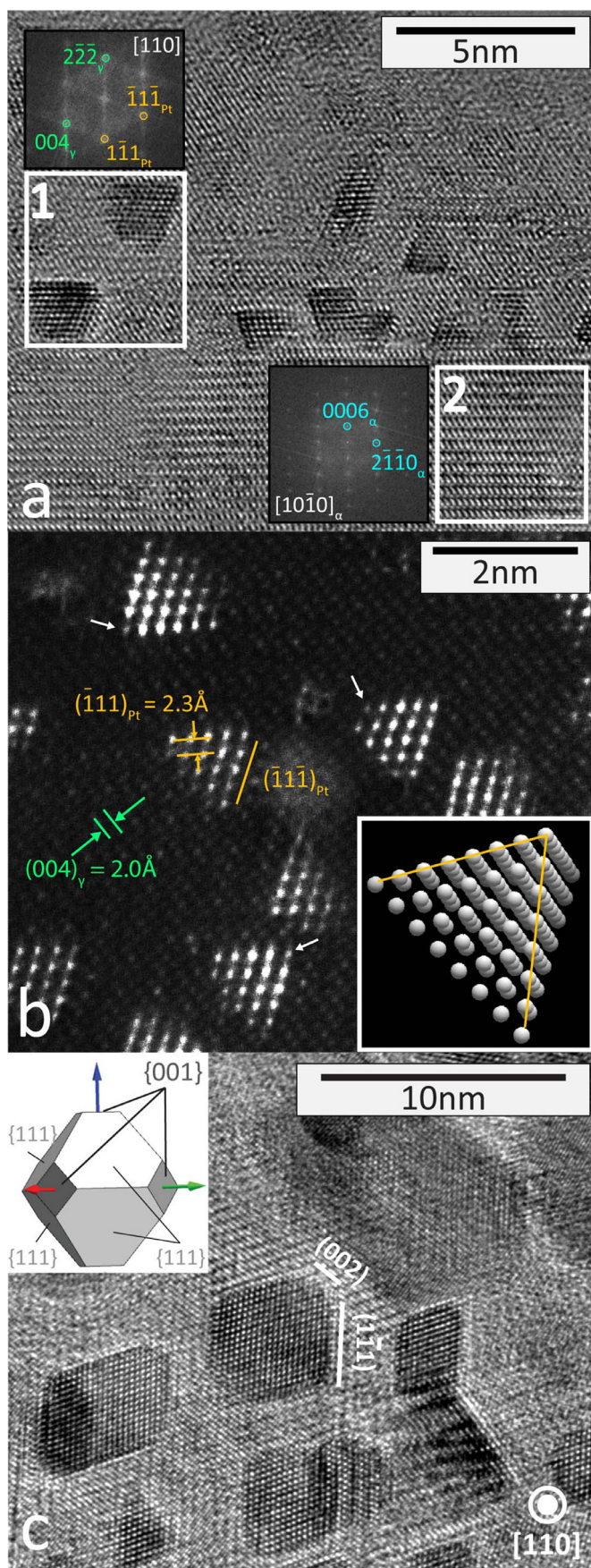
single crystals, took on two orientations. One interfacial relationship was the "cube-on-cube" orientation observed here, the other was reported as $Pt(100)[011]||\gamma$-$Al_2O_3(111)[211]$, which was not observed in this study. The common $(111)_{Pt}||(111)_\gamma$; $[1\bar{1}0]_\gamma||[1\bar{1}0]_{Pt}$ interface is the focus of current atomic-resolution characterization.

Ion implantation followed by thermal annealing has been used to synthesize transition aluminas, including ones with embedded metal nanoparticles, but the method has not seen its full potential in the study of the interfacial structure of systems that are important for catalysis. Although the processing path differs from those used to produce supported industrial catalysts, it offers a high degree of control over the purity of the system and allows the system to access degrees of freedom in the formation of interfacial relationships that are not possible with processing methods that entail deposition of Pt or a Pt-containing precursor on γ-alumina. Use of a processing path where the Pt precipitates into alumina as it crystallizes removes the biasing effect of a pre-existing γ-alumina surface structure by removing pre-existing surface orientations.

Although diffusion in alumina is expected to be sluggish at the processing temperature used here, Pt nanoprecipitates with atomically sharp interfaces were formed in experimentally accessible times, when high ion implantation fluences were used. With a larger survey of nanoparticles, this model system provides a means to compare the relative contributions of edge energy [35,36], strain [37,38], and interfacial chemistry on the energetics of the system. The interfacial energies for different chemical terminations of the {111} faceted interfaces have been calculated [41], guided by the experimental observation of the interfaces here, but further data is needed on {200} interfaces and edge energies.

Declaration of Competing Interest

The authors declare that they have no known competing financial interests or personal relationships that could have appeared to influence the work reported in this paper.

Acknowledgements

Fig. 4. Aberration-corrected phase-contrast HRTEM (a,c) and probe-corrected HAADF STEM (b) micrographs of the 1×10^{17} Pt/cm^2 implanted wafer after 800 °C at 500 h. The FFT of region 1 in (a) is consistent with the cube-on-cube orientation between Pt and γ-alumina. The FFT of region 2 shows that γ-alumina crystallizes epitaxially from the α-alumina with the orientation $(0001)_\alpha||(111)_\gamma$; $[10\bar{1}0]_\alpha||[110]_\gamma$. The 3D morphology of Pt nanoparticles may be more easily inferred from the HAADF STEM image. The inset shows a model of a perfect tetrahedral Pt nanoparticle bound by {111} facets tilted slightly off the [110] zone axis; the low intensity at the corners of the nanoparticles in the STEM images indicate "missing" corner and edge atoms (indicated by white arrows) which are not shown in the model. Larger Pt nanoparticles (c) tend to be cubo-octahedral rather than tetrahedral. A 3-D model is shown in the inset [42].

References

[1] A. Meldrum, R.F. Haglund, L.A. Boatner, C.W. White, Adv. Mater. 13 (2001) 1431–1444.
[2] P. Normand, E. Kapetanakis, P. Dimitrakis, D. Skarlatos, K. Beltsios, D. Tsoukalas, C. Bonafos, G. Ben Assayag, N. Cherkashin, A. Claverie, J.A. Van Den Berg, V. Soncini, A. Agarwal, M. Ameen, M. Perego, M. Fanciulli, Nucl. Inst. Methods Phys. Res. Section B-Beam Interact. Mater. Atoms 216 (2004) 228–238.
[3] J.D. Budai, C.W. White, S.P. Withrow, M.F. Chisholm, J. Zhu, R.A. Zuhr, Nature 390 (1997) 384–386.
[4] C.W. White, S.P. Withrow, J.D. Budai, L.A. Boatner, K.D. Sorge, J.R. Thompson, K.S. Beaty, A. Meldrum, Nucl. Instrum. Methods B 191 (2002) 437–441.
[5] M.K. Santala, V. Radmilovic, R. Giulian, M.C. Ridgway, R. Gronsky, A.M. Glaeser, Acta Mater 59 (2011) 4761–4774.
[6] M. Trueba, S.P. Trasatti, Eur. J. Inorg. Chem. (2005) 3393–3403.
[7] G. Ertl, H. Knözinger, J. Weitkamp, The Handbook of Heterogeneous Catalysis, Wiley-VCH, Weinheim, 1997.
[8] A. Ionescu, A. Allouche, J.P. Aycard, M. Rajzmann, F. Hutschka, J. Phys. Chem. B 106 (2002) 9359–9366.
[9] J.C. Vedrine, Catalysts 7 (2017).
[10] K. Wefers, C. Misra, Oxides and Hydroxides of Aluminum: alcoa Technical Paper No. 19, Revised Alcoa Laboratories, 1987.
[11] I. Levin, D. Brandon, J. Am. Ceramic Soc. 81 (1998) 1995–2012.
[12] R.S. Zhou, R.L. Snyder, Acta Crystallographica Section B-Struct. Sci. 47 (1991) 617–630.
[13] C. Pecharroman, I. Sobrados, J.E. Iglesias, T. Gonzalez-Carreno, J. Sanz, J. Phys. Chem. B 103 (1999) 6160–6170.
[14] L. Samain, A. Jaworski, M. Eden, D.M. Ladd, D.K. Seo, F.J. Garcia-Garcia, U. Haussermann, J. Solid State Chem. 217 (2014) 1–8.
[15] C. Wolverton, K.C. Hass, Phys. Rev. B 6302 (2001) 024102.
[16] M. Digne, P. Sautet, P. Raybaud, P. Euzen, H. Toulhoat, J. Catal. 211 (2002) 1–5.
[17] G. Paglia, C.E. Buckley, A.L. Rohl, B.A. Hunter, R.D. Hart, J.V. Hanna, L.T. Byrne, Phys. Rev. B 68 (2003).
[18] M. Digne, P. Sautet, P. Raybaud, P. Euzen, H. Toulhoat, J. Catal. 226 (2004) 54–68.
[19] G. Paglia, A.L. Rohl, C.E. Buckley, J.D. Gale, Phys. Rev. B 71 (2005).
[20] K.J. Morrissey, K.K. Czanderna, R.P. Merrill, C.B. Carter, Ultramicroscopy 18 (1985) 379–385.
[21] I. Levin, T. Gemming, D.G. Brandon, Physica Status Solidi a-Appl. Res. 166 (1998) 197–218.
[22] L. Kovarik, M. Bowden, A. Genc, J. Szanyi, C.H.F. Peden, J.H. Kwak, J. Phys. Chem. C 118 (2014) 18051–18058.
[23] L. Kovarik, M. Bowden, D.C. Shi, N.M. Washton, A. Andersen, J.Z. Hu, J. Lee, J. Szanyi, J.H. Kwak, C.H.F. Peden, Chem. Mater. 27 (2015) 7042–7049.
[24] L. Kovarik, A. Genc, C.M. Wang, A.N. Qiu, C.H.F. Peden, J. Szanyi, J.H. Kwak, J. Phys. Chem. C 117 (2013) 179–186.
[25] M.K. Santala, V. Radmilovic, R. Giulian, M.C. Ridgway, A.M. Glaeser, R. Gronsky, Scr. Mater. 62 (2010) 187–190.
[26] M.K. Santala, On Orientation Relationships and Morphologies of Platinum Precipitates in Sapphire, Mater. Sci. Eng., vol. Ph.D., University of California, Berkeley, 2009.
[27] M. Gandman, M. Ridgway, R. Gronsky, A.M. Glaeser, Acta Mater. 83 (2015) 169–179.
[28] N. Yu, P.C. McIntyre, M. Nastasi, K.E. Sickafus, Phys. Rev. B 52 (1995) 17518–17522.
[29] C.W. White, C.J. McHargue, P.S. Sklad, L.A. Boatner, G.C. Farlow, Mater. Sci. Rep. 4 (1989) 41–146.
[30] E. Alves, R.C. da Silva, O. Conde, M.F. da Silva, J.C. Soares, Nucl. Inst. Methods B 148 (1999) 1049–1053.
[31] C.W. White, S.P. Withrow, K.D. Sorge, A. Meldrum, J.D. Budai, J.R. Thompson, L.A. Boatner, J Appl Phys 93 (2003) 5656–5669.
[32] J.F. Ziegler, M.D. Ziegler, J.P. Biersack, Nucl. Inst. Methods Phys. Res. Section B-Beam Interact. Mater. Atoms 268 (2010) 1818–1823.
[33] L.R. Doolittle, Nucl. Inst. Methods Phys. Res. Section B-Beam Interact. Mater. Atoms 9 (1985) 344–351.
[34] N.P. Barradas, K. Arstila, G. Battistig, M. Bianconi, N. Dytlewski, C. Jeynes, E. Kotai, G. Lulli, M. Mayer, E. Rauhala, E. Szilagyi, M. Thompson, Nucl. Inst. Methods Phys. Res. Section B-Beam Interact. Mater. Atoms 262 (2007) 281–303.
[35] L.D. Marks, Surf. Sci. 150 (1985) 358–366.
[36] L.D. Marks, Rep. Progr. Phys. 57 (1994) 603–649.
[37] U. Dahmen, S.Q. Xiao, S. Paciornik, E. Johnson, A. Johansen, Phys. Rev. Lett. 78 (1997) 471–474.
[38] M.E. Thompson, C.S. Su, P.W. Voorhees, Acta Metallurgica Et Materialia 42 (1994) 2107–2122.
[39] P. Wynblatt, D. Chatain, J. Mater. Sci. 52 (2017) 9630–9639.
[40] Z. Zhang, L. Li, J.C. Yang, J. Phys. Chem. C 117 (2013) 21407–21412.
[41] K. Oware Sarfo, A.L. Clauser, M.K. Santala, L. Árnadóttir, Appl. Surf. Sci. (submitted 2020, in review).
[42] R.V. Zucker, D. Chatain, U. Dahmen, S. Hagege, W.C. Carter, J. Mater. Sci. 47 (2012) 8290–8302.